JOURNAL OF MATERIALS SCIENCE **37** (2002) 1135–1142

Hot corrosion of Fe_3Al

D. DAS, R. BALASUBRAMANIAM*, M. N. MUNGOLE
Department of Materials and Metallurgical Engineering, Indian Institute of Technology, Kanpur 208016, India
E-mail: bala@iitk.ac.in

The oxidation and hot corrosion behavior of the binary iron aluminide, Fe-25Al (at.%), has been studied at 1100 K, 1225 K and 1330 K. Hot corrosion studies were conducted by coating the specimen surfaces with 2.5 ± 0.2 mg/cm^2 of Na_2SO_4 prior to exposure in pure oxygen. Parabolic rate constants were obtained from weight gain data. The faster kinetics in the initial stages of oxidation have been related to the formation of θ-Al_2O_3 and the slower kinetics in the later stages of oxidation, to the formation of α-Al_2O_3. The overall rate of hot corrosion was higher than that of oxidation at all the temperatures. The presence of α-Fe_2O_3 in addition to alumina was indicated by XRD analysis of the scales present on the surface of the samples after hot corrosion. FTIR spectra from the spalled scales in hot corrosion divulged the presence of α-Al_2O_3, α-Fe_2O_3 and sulfate. Cross-sectional microscopy revealed that the metal-scale interfaces were pitted in hot corrosion conditions and the pits contained aluminum sulfide. Sulfides were also identified along the grain boundaries in the intermetallic near the scale-metal interface. The hot corrosion process has been explained based on sulfide formation and its subsequent oxidation.

1. Introduction

Iron aluminides are ordered intermetallics centered around compositions Fe_3Al and FeAl. They possess relatively high specific strengths and suitable mechanical properties at elevated temperatures. Fe_3Al-based iron aluminides contain aluminum well in excess of the critical levels (14 at.% Al) for external scale formation and hence the scale formed is essentially alumina [1, 2]. The soundness and adherence of Al_2O_3 scale to the underlying alloy, therefore, determine the actual high temperature oxidation and corrosion behavior. At lower temperatures (below 1200 K), the scale consists of transitional alumina (γ-, δ-, and θ-Al_2O_3) while, at higher temperatures, the scale consists of the stable form of alumina, namely α-Al_2O_3 [3, 4]. Transition aluminas, like θ-Al_2O_3, have also been reported by some investigators, during the transient stages of oxidation and at intermediate temperatures [5–9]. The faster oxidation kinetics at lower temperatures have been explained based on the formation of θ-Al_2O_3 [5–9]. Transition aluminas like θ-Al_2O_3 have structures similar to γ-Al_2O_3 (i.e. cubic structure) with variation in the ordering of cation vacancies [6]. The different forms of alumina also possess characteristic microstructures. At lower temperatures, the θ-Al_2O_3 structure is a combination of nodules and whiskers, while, at the higher temperatures, the nodules or whiskers are less apparent [10]. Smialek *et al.* [5] observed a distinct, whisker-type morphology for the fast-growing θ-Al_2O_3. Higher temperature oxidation produced spheroidization and coarsening of the residual whisker morphology and the appearance of concave cells. Scale spalling was more enhanced at lower temperatures and this was related to the presence of transitional alumina [11]. It has been explained that, when θ-Al_2O_3 forms, scale spallation occurred due to void formation at the oxide-metal interface [6]. Whiskers of θ-Al_2O_3 were found on top of ridges of α-Al_2O_3 in the intermediate temperature range [8]. High resolution TEM [12] has shown that the stable α-Al_2O_3 nucleated at the oxide-metal interface and grew into the metal, thereby filling up the voids. This results in reduced scale spallation and improved adherence, and therefore, the formation of α-Al_2O_3 is preferred. Under the spalled outer θ-Al_2O_3 scale, underlying α-Al_2O_3 ridges were present [11]. Transformation of the transitional phases to stable α-Al_2O_3 results in a ridged morphology and a reduction in oxidation rate [6]. The sequence of formation of aluminas in alumina-forming intermetallics has been described elsewhere [6, 13].

Limited literature is available for hot corrosion of Fe-Al systems in Na_2SO_4 melts, whereas their sulphidation has been widely reported. The presence of molten alkali sulfate salts significantly increased the corrosion of iron aluminides in SO_2-containing mixed gases [14]. A coating of $Na_2SO_4 - Li_2SO_4$ on iron aluminides exposed to an oxidizing/sulphidizing gaseous environment (1% SO_2 in air) at 605°C and 800°C resulted in corrosion rates that were at least ten times higher than rates measured in the absence of the sulfate

*Author to whom all the correspondence should be addressed.

coating [14]. The degradation by the molten sulfate decreased with increasing Cr contents (2% to 5%) and increasing Al contents (28% to 36%). Stainless steels (310 and 321) possessed significantly better hot corrosion resistance than iron aluminides [14]. In another study by Gesmundo *et al.* [15], both Fe_3Al (27Al-2.2Cr-0.1B) and FeAl (40Al-0.05Zr-0.06B-0.085C) alloys were coated with Na_2SO_4-containing salts and exposed to a simulated combustion gas at 600°C. Recently, Medina *et al.* [16] studied the hot corrosion of Fe-40Al, Fe-40Al + 0.1B and Fe-40Al + 0.1B + $10Al_2O_3$ alloys in molten $NaVO_3$ at 625°C and 700°C by potentiodynamic polarization. Both these studies indicated that the surface alumina scale was attacked by the sulfate-containing salts, resulting in enhanced degradation and in oxidation of the other major element in the alloys, i.e. Fe. The aim of the present study is to understand the sodium sulfate induced hot corrosion of stoichiometric Fe_3Al.

2. Experimental procedure

The Fe-25Al (exact composition 74.72Fe-25.28Al ± 0.25) intermetallic was obtained from the Defense Metallurgical Research Laboratory (DMRL), Hyderabad. Rectangular specimens were sectioned, mechanically polished to 600-grit and degreased using acetone and alcohol. Thermogravimetric technique was employed for kinetic measurements. The apparatus consisted of a vertical furnace, a Mettler single pan analytical balance, and gas train. A vertical furnace of 250 mm length was employed to conduct the oxidation and hot corrosion tests. A mullite tube (45 mm inner diameter and 460 mm length) acted as the reaction chamber. The specimen was placed inside a quartz crucible constructed with three holes at the bottom of the crucible to allow for passage of gas. The crucible was 15 mm in diameter and 20 mm in length. The quartz crucible was suspended from the top of the furnace using a platinum wire into the reaction zone of the reaction chamber. Pure oxygen gas was passed initially through a bubbler and capillary flow meter, and then through Ascarite, anhydrous calcium chloride and Drierite ($CaSO_4$) columns successively before introduction into the reaction chamber. The outlet gas was passed through a bubbler to ensure that the flow of gas was maintained through the system.

Oxidation and hot corrosion experiments were carried out isothermally at temperatures of 1100 K, 1225 K and 1330 K. The gas flow rate was maintained constant at 0.2 cm^3/s (STP). The quartz crucible was periodically removed from the furnace, the weight of the sample recorded and the crucible again reintroduced into the furnace. For the hot corrosion experiments, the specimens were initially coated with a thin film of Na_2SO_4 and then exposed to the environment at the desired temperature. The salt deposit was applied to the warm (~150°C) specimen using a brush, to give a uniform coat of the aqueous solution of Na_2SO_4 on the surface of the specimen. A surface coverage of 2.5 mg/cm^2 of salt was used [17]. The kinetics of hot corrosion were monitored by measuring the weight changes as a function of time, similar to the oxidation experiments. There was noticeable scale spallation at the two higher temperatures. The spalled scales were collected and weighed with the specimen.

The corrosion products were visually observed to record scale color, adherence and uniformity. X-ray diffraction (XRD) patterns were obtained from the surface scales with a Rich-Seifert 2002D diffractometer using Cu K_α radiation. A JEOL JSM 840A scanning electron microscope (SEM) was employed for topological observation of the surface. A JEOL JXA-8600MX electron probe micro-analyzer (EPMA) was utilized for qualitative compositional analyses. The cross-sections were studied after electroless nickel plating the surfaces and mounting the cross-sections in epoxy resin. The mounted specimens were polished and etched with $HNO_3 + CH_3COOH + H_2O + HF$ (33 : 33 : 33 : 1) before observation of the cross-section. The oxidation and hot corrosion products from select experiments were analyzed by Fourier transform infrared (FTIR) spectroscopy after pressing them into pellets using spectroscopically pure KBr. The FTIR spectra were recorded at room temperature using a Nicolet Magna 750 Series 2, FTIR system.

3. Results

3.1. Kinetics

The parabolic rate constant k_p was obtained from the slope of the linear regression fitted line of $(\Delta W/A)^2$ vs. t plot. Figs 1 and 2 shows the nature of fit of

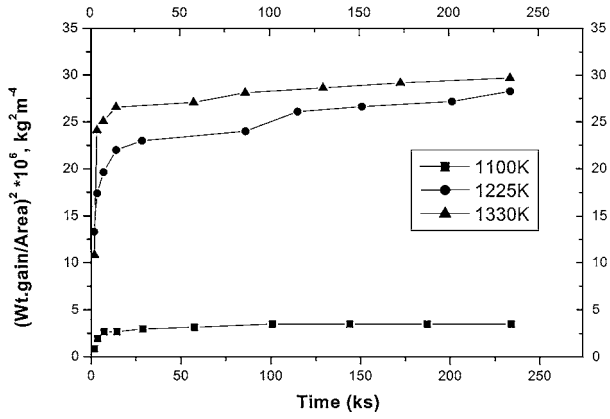

Figure 1 $(\Delta W/A)^2$ vs. time plots for oxidation of Fe-25Al in pure oxygen. The lines joining the data points are for visual aid only.

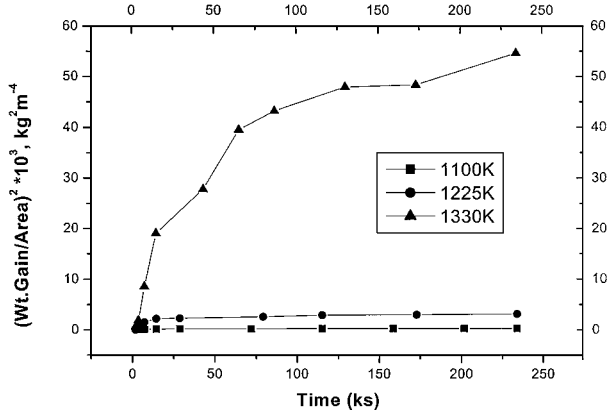

Figure 2 $(\Delta W/A)^2$ vs. time plots for hot corrosion of Fe-25Al in pure oxygen. The lines joining the data points are for visual aid only.

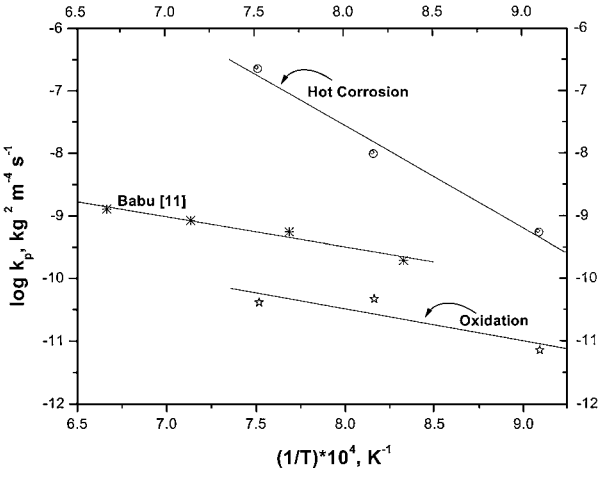

Figure 3 Variation of overall parabolic rate constant (k_p) with temperature for the oxidation and hot corrosion experiments. The k_p determined for the oxidation of Fe-25Al in oxygen by Babu *et al.* [12] by continuous weight gain method have also been presented. The lines joining the data points are for visual aid only.

parabolic rate law for the oxidation and hot corrosion experiments, respectively. Ideally, parabolic growth would yield straight lines on such plots, with the slope being equal to the rate constant k_p. It may be noticed from Figs 1 and 2 that the obedience to parabolic rate law was only approximate. This is due to the discontinuous method of recording weight gain. In the case of oxidation, the nature of the plot (Fig. 1) indicated two regions where different parabolic rate constants applied; one encompassing the initial stages of oxidation (up to 2 hours approximately) and the other, the later stages of oxidation. Parabolic rate constants, k_{pI} and k_{pII}, were determined from these initial and final stages, respectively. These rate constants will be addressed later in the discussion section. The overall rate parabolic rate constants were determined for the oxidation and hot corrosion experiments by utilizing all the data points of the experiment. The variation of the overall parabolic rate constants with temperature is presented in Fig. 3. In the same figure, the rate constants reported by Babu *et al.* [11] for the oxidation of the Fe-25Al alloy in oxygen have been provided. Babu *et al.* [11] monitored the progress of oxidation by recording the continuous weight gains using a Cahn 1000 electrobalance. The activation energies implied from the slopes of the curves are not relevant because, as noted above, true parabolic kinetics were not obeyed in the present set of experiments.

3.2. Scale characterization

Visual observation of the scales revealed that the color of scales after oxidation at 1225 K and 1330 K was cream white, while the scale after oxidation at 1100 K was dull white. The spalled scales in the oxidation experiments, especially at the lower temperature, were in the form of loose fine powders of white color. Severe scale spalling was noted for the hot corroded samples, mainly at the two higher temperatures (1330 K and 1225 K). The color of the spalled scale was deep brown. The salt did not melt at 1100 K and spalled as a loose dry mass. A white layer of loose scales in all the cases covered the sample surface (from where the scale had spalled off).

Analysis of the XRD patterns of all the specimens after oxidation revealed that θ-Al_2O_3 was the major phase at the lowest oxidation temperature of oxidation. At the intermediate temperature, α-Al_2O_3 was present in addition to θ-Al_2O_3, with the former being the major phase. At the highest temperature, the major constituent of the scale was α-Al_2O_3. In the hot corrosion specimens, the types of Al_2O_3 phases observed were similar to those observed after the oxidation experiments. In addition, peaks corresponding to α-Fe_2O_3 were identifiable after hot corrosion at 1225 K and 1330 K. FTIR spectra from the scales of the oxidized specimens confirmed the presence of alumina. The spectra from the spalled scales after hot corrosion at 1225 K and 1330 K indicated the presence of α-Fe_2O_3 and sulfate, in addition to alumina, for both the alloys. The scale characterization results are summarized in Table I.

The scale after oxidation at 1100 K revealed fine faceted oxides (Fig. 4a). At higher temperatures, a ridge-like morphology developed (Fig. 4b and c). In the case of hot corrosion, the specimens were generally covered with uniform scales. Nodular features were observed on the surface at 1100 K (Fig. 5a), while a ridge-like morphology could be discerned at 1225 K (Fig. 5b). At 1330 K, the surface exhibited large nodular features (Fig. 5c) surrounded by clusters of fine needle-like whiskers. EPMA analysis of the whiskers confirmed Al_2O_3. The whisker morphology of the alumina revealed that it was θ-Al_2O_3 [8]. Therefore, the morphology of alumina formed after hot corrosion was different from that after oxidation at 1330 K.

4. Discussion

4.1. Oxidation

The oxidation kinetics were analyzed with two distinct parabolic behaviors, as noted earlier. The parabolic rate

TABLE I Summary of nature of scales observed after oxidation (OX) and hot corrosion (HC)

Condition	Temp. (K)	Phases identified by XRD		FTIR identification	Scale characteristics
		Major	Minor		
OX	1100	θ-Al_2O_3	–	–	Dull white
	1225	α-Al_2O_3	θ-Al_2O_3	–	Cream white
	1330	α-Al_2O_3	–	γ-FeOOH, α-Al_2O_3	Cream white
HC	1100	θ-Al_2O_3	–	–	Dull brown
	1225	α-Al_2O_3	θ-Al_2O_3, α-Fe_2O_3	Na_2SO_4, α-Al_2O_3, α-Fe_2O_3	Brown
	1330	α-Al_2O_3	α-Fe_2O_3	Na_2SO_4, α-Al_2O_3, α-Fe_2O_3	Brown

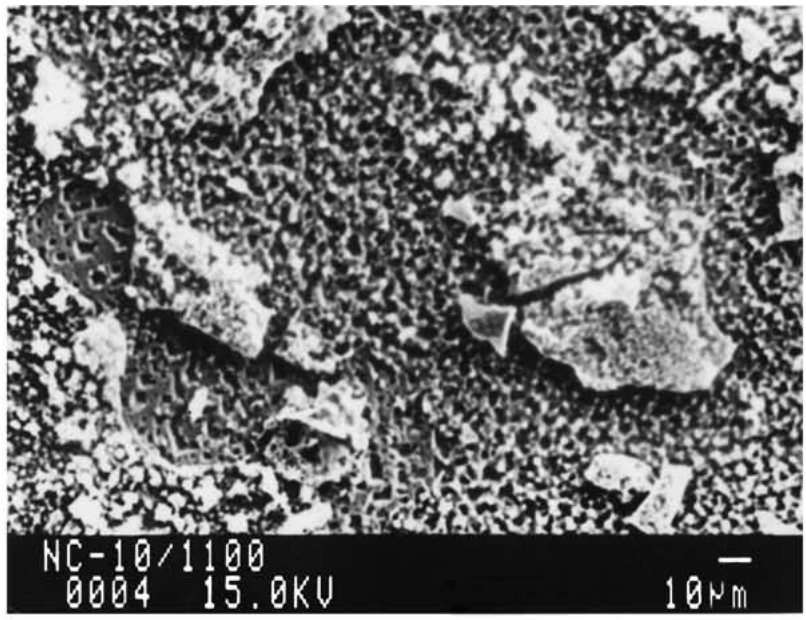

(a)

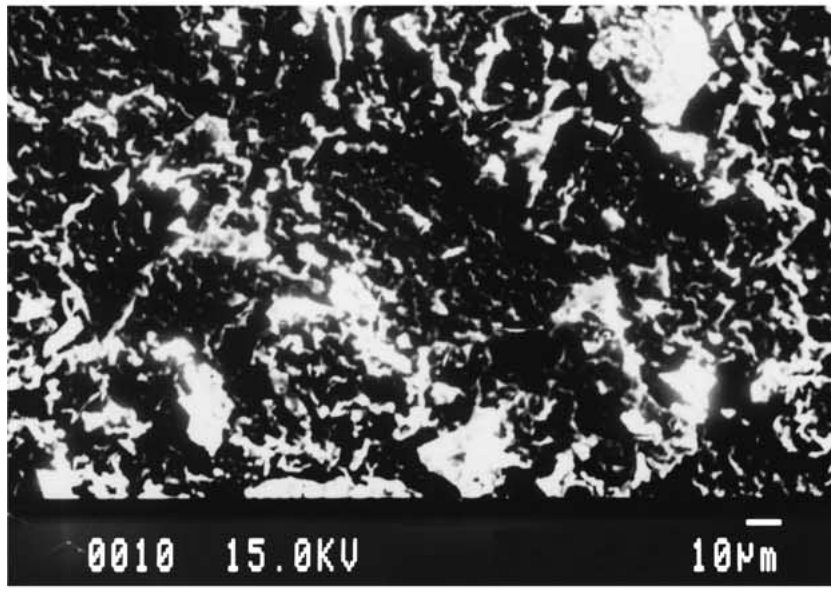

(b)

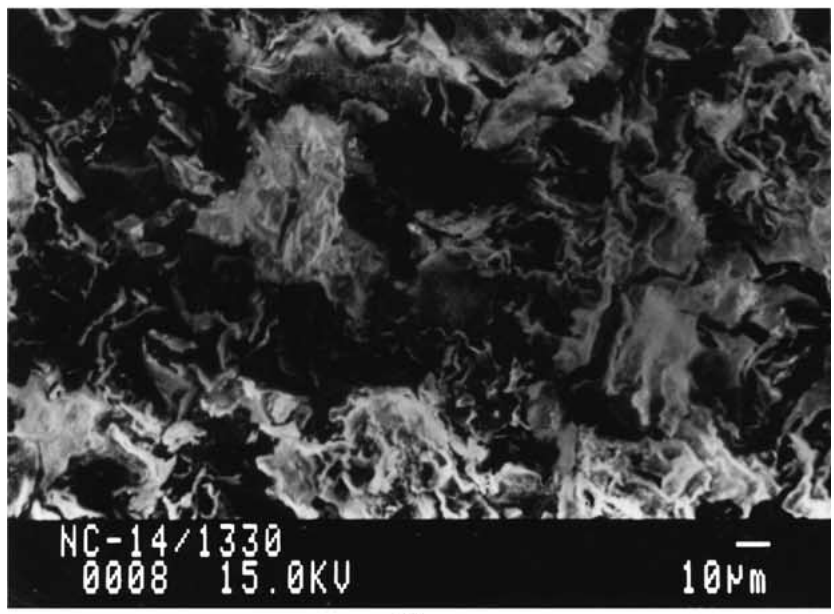

(c)

Figure 4 SEM morphologies of the oxide scales after oxidation for 65 hrs at (a) 1100 K, (b) 1225 K, and (c) 1330 K.

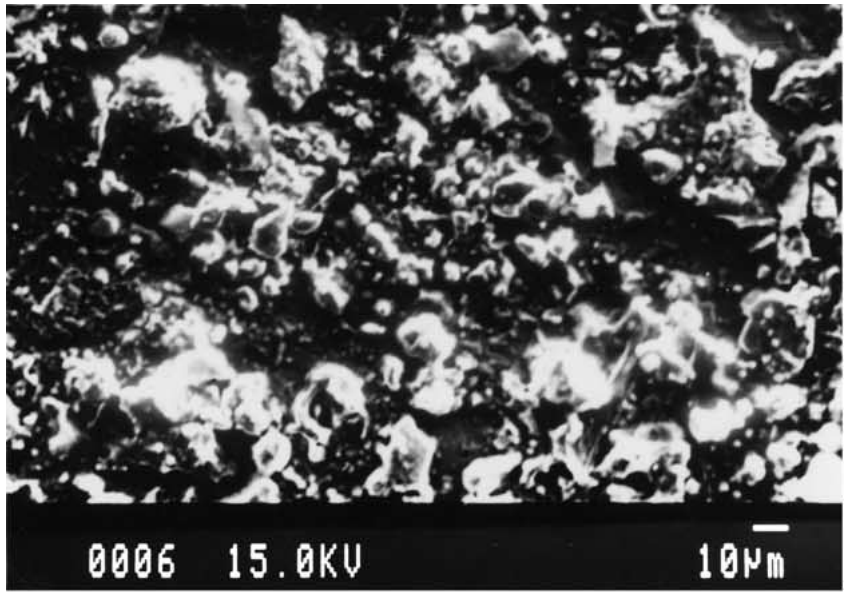

(a)

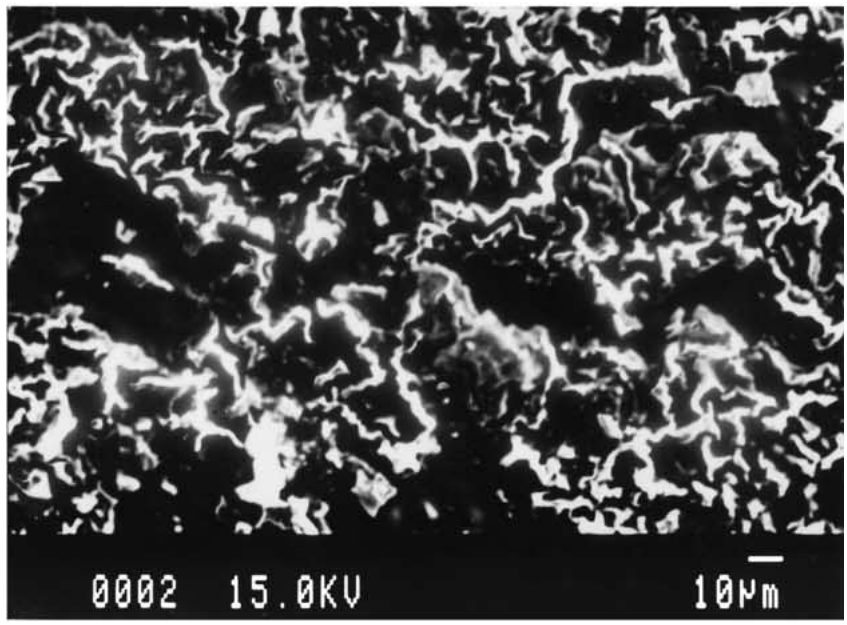

(b)

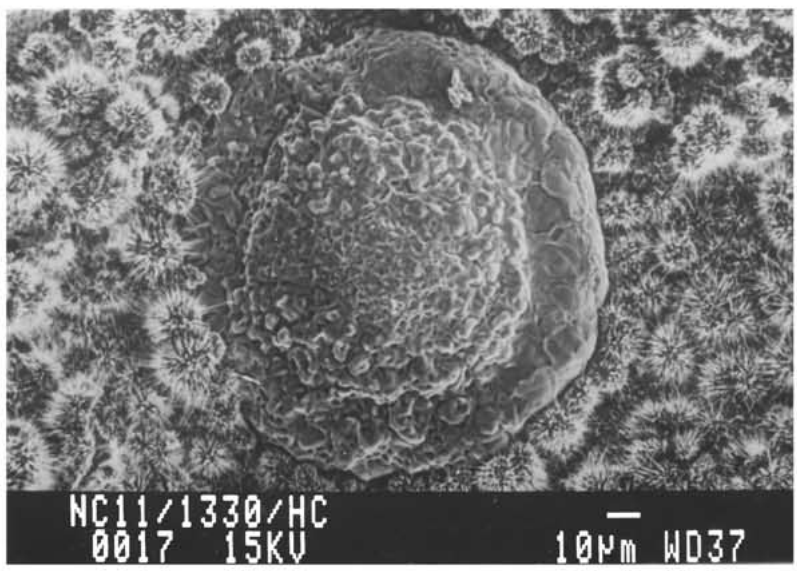

(c)

Figure 5 SEM morphologies of the scales after hot corrosion for 65 hours at (a) 1100 K, (b) 1225 K, and (c) 1330 K.

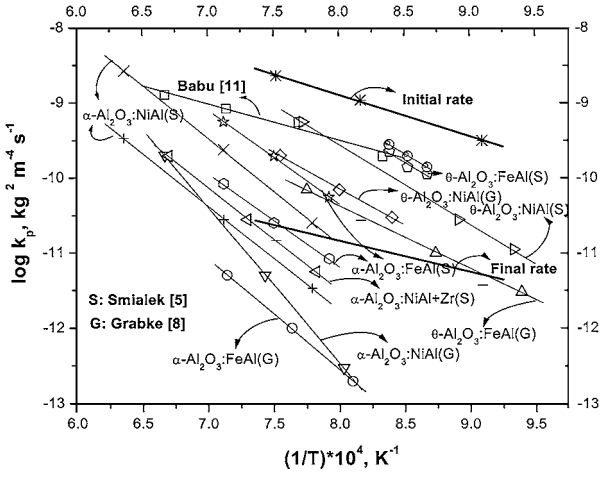

Figure 6 Literature data [5, 7, 8, 10] for kinetics of α- and θ-Al_2O_3 formation. The parabolic oxidation rate in the initial (k_{pI}) and final (k_{pII}) periods for the alloy Fe-25Al has been provided.

constants in the initial stages of oxidation were higher than in the later stages at all the temperatures. It was earlier pointed by Rommerskirchen *et al.* [8] that the oxidation kinetics of iron aluminides could be analyzed as consisting of two regions of parabolic behavior and they correlated these regions to the formation of different kinds of alumina. For example, the faster initial oxidation kinetics were related to the formation of transition θ-Al_2O_3 while the lower oxidation kinetics in the later stages were related to α-Al_2O_3 formation [8]. The parabolic rate constants obtained in the present study for the two different regions are compared with α- and θ-Al_2O_3 formation kinetics [5, 7, 8, 10] in Fig. 6. The initial rate can be related to θ-Al_2O_3 formation kinetics while the rate from the later stages of oxidation can be related to α-Al_2O_3 formation kinetics. The analysis of the weight gain data obtained by grouping them into two regions is justified in the present case because XRD results clearly revealed that two types of alumina form during oxidation. The scale nature was determined using XRD based on the remaining oxide on the surface. It must be pointed out that the variation in oxide formation as a function of oxidation time was not determined, due to scale spallation. The scale nature identified at the end of the experiments need not match the scale nature throughout the course of the experiment. While the major alumina phase identified at the lowest temperature was θ-Al_2O_3, the major alumina phase determined by XRD was α-Al_2O_3 at higher temperatures. It was earlier seen that the transitional alumina (θ-Al_2O_3) forms first and later transforms to α-Al_2O_3 and this occurs more readily at higher temperature [12]. Therefore, the presence of θ-Al_2O_3 on the surface after long oxidation times is more likely at lower oxidation temperatures.

4.2. Hot corrosion

The hot corrosion rates were higher than oxidation rates at all the temperatures. Cross sectional microscopy revealed that the surface scale was thicker after hot corrosion (Fig. 7a). The penetration of a corrosion zone can be noted. EPMA analysis of the corrosion product zone revealed that the product consisted essentially of Fe_2O_3 and Al_2O_3. Similar penetrating corrosion product zones were not consistently observed on all surfaces. However, the region below the metal-scale interface was consistently pitted and these pits contained corrosion products (Fig. 7b). The corrosion products in the pits at the scale-metal interface were analyzed qualitatively by EPMA and found to contain significant amounts of S in addition to Fe and Al. The EPMA results obtained from the scale in the same sample did not reveal any S but only Al, Fe and O. When considered along with the XRD results, it can be concluded that the external scales were composed of α-Fe_2O_3 and α-Al_2O_3. The corrosion products within the pits were sulfides. The identification of sulfur at the scale-metal interface showed that sulfur-bearing compounds are found deeper in the material below the scale. Significant presence of corrosion products was also constantly noticed along grain boundaries in the matrix near the scale-metal interface (Fig. 7b). The corrosion products in the pits along the grain boundary in Fig. 7b were analyzed qualitatively by EPMA as aluminum sulfide. The base metal was degraded in a characteristic fashion at the scale-metal interface, where deep pits could be observed at the interface (Fig. 7b). Interestingly, the inner scale near the scale-metal interface in the Fe-27Al-2.2Cr-0.1B alloys after Na_2SO_4 induced hot corrosion in a SO_2-containing environment at 600°C revealed the presence of Al_2O_3, Al_2S_3 and some Fe [15].

Some aspects about the process of hot corrosion can be understood based on the microstructural and compositional characterization, when viewed along with the known mechanisms of hot corrosion. The identification of sulfate in the spalled scales by FTIR spectroscopy indicates the significance of the acid fluxing mechanism in the initial stages of hot corrosion [18]. Fe_2O_3 was identified in the spalled scales only at the two higher temperatures. Therefore, non-protective surface conditions were established when Na_2SO_4 melted on the surface (melting point 884°C), which resulted in the oxidation of both Al and Fe. The results of the present study, that both Al_2O_3 was Fe_2O_3 occurred as corrosion products during hot corrosion, are in agreement with other hot corrosion studies of iron aluminides [15, 16]. Sustained, accelerated hot corrosion induced by Na_2SO_4 appears to be associated with sulfide formation at or near the scale-metal interface. The sulfide phases provide path for rapid outward diffusion of the metal. A notable feature of attack by this mechanism is the formation of pits at the scale-metal interface [19], and this was also observed in the present study by cross sectional microscopy. The identification of aluminum sulfides in the pits suggests probably that sulphidation of Al results in non-protective scale formation because Al is the metal that is required to form the protective oxide in iron aluminides. The sulfur released after oxidation of the sulfides diffuses inside the material, faster through the grain boundaries, to cause further degradation.

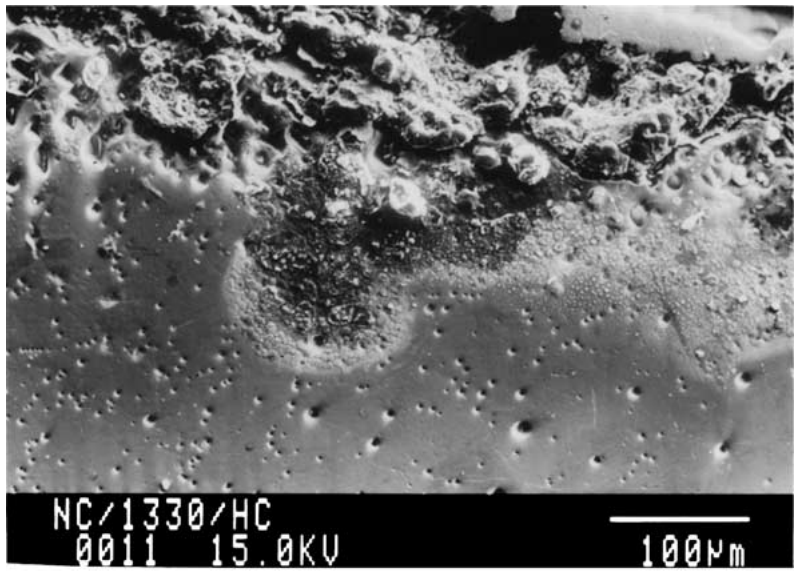

(a)

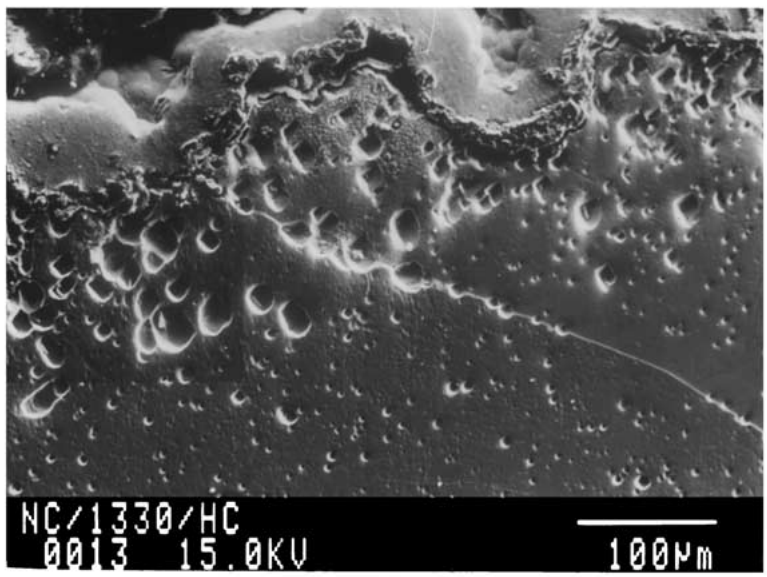

(b)

Figure 7 SEM morphologies of the cross-sectional features hot corroded at 1330 K for 65 hrs (a) at one location and (b) at another location.

5. Conclusions

The high temperature oxidation and hot corrosion behavior at 1100 K, 1225 K and 1330 K of Fe-25Al has been studied. The weight gain data were analyzed assuming parabolic kinetics. The kinetics of hot corrosion were generally faster than oxidation. Cross-sectional microstructural analysis revealed pitting just below the scale-metal interface and enhanced attack along grain boundaries in the underlying metallic matrix. The external scales contained essentially Al_2O_3 after the oxidation experiments, whereas both Fe_2O_3 and Al_2O_3 were identified after hot corrosion experiments at higher temperatures. Qualitative compositional analysis by an EPMA indicated the presence of aluminum sulfides in the pits at the scale-metal interface, and in the pits along the grain boundaries in the metallic matrix below the scale-metal interface. The faster hot corrosion kinetics has been attributed to the formation of sulfides at the scale-metal interface. The possible sequence of attack in hot corrosion has been proposed based on microstructural and compositional analyses. Fluxing of alumina results in higher attack rates. The formation of aluminum sulfides results in non-protective scales. The oxidation of sulfides releases sulfur, which again diffuses inward into the material to cause further attack.

Acknowledgements

The authors thank Drs. D. Banerjee and R. Baligdad of Defense Metallurgical Research Laboratory (DMRL), Hyderabad for providing the specimens used in the present study. The authors also thank Dr. A. V. Ramesh Kumar of the Defense Materials Stores Research and Development Establishment (DMSRDE), Kanpur for performing the FTIR spectroscopic studies.

References

1. P. TOMASZEWICZ and G. WALLWORK, *Rev. High Temp. Mater.* **4** (1978) 75.
2. *Idem.*, *Oxid. Met.* **19** (1983) 165.
3. P. F. TORTORELLI and J. H. DEVAN, *Mater. Sci. Eng.* A **153** (1992) 573.
4. R. PRESCOTT and M. J. GRAHAM, *Oxid. Met.* **38** (1992) 73.

5. J. L. SMIALEK, J. DOYCHAK and D. J. GAYDOSH, in "Oxidation of High Temperature Intermetallics," edited by T. Grobstein and J. Doychak (TMS, Warrendale, PA, 1988) p. 83.
6. J. DOYCHAK, in "Intermetallic Compounds," edited by J. H. Westbrook and R. L. Fleischer (Wiley, New York, 1994) p. 977.
7. J. L. SMIALEK, H. DOYCHAK and D. J. GAYDOSH, *Oxid. Met.* **34** (1990) 259.
8. I. ROMMERSKIRCHEN, B. ELTESTER and H. J. GRABKE, *Materials and Corrosion* **47** (1996) 646.
9. B. A. PINT, P. F. TORTORELLI and I. G. WRIGHT, in "Oxidation of Intermetallics," edited by H. J. Grabke and M. Schütze (Wiley-VCH, Weinheim, 1997) p. 183.
10. G. C. RYBICKI and J. L. SMIALEK, *Oxid. Met.* **31** (1989) 275.
11. N. BABU, R. BALASUBRAMANIAM and A. GHOSH, *Corrosion Science* **43** (2001) 2239.
12. E. SCHUMANN, J. C. YANG, M. J. GRAHAM and M. RÜHLE, in "Oxidation of Intermetallics," edited by H. J. Grabke and M. Schütze (Wiley-VCH, Weinheim, 1997) p. 121.
13. R. KLUMPES, C. H. M. MAREE, E. SCHRAMM and H. H. W. DE WIT, in "Oxidation of Intermetallics," edited by H. J. Grabke and M. Schütze (Wiley-VCH, Weinheim, 1997) p. 99.
14. W. H. LEE and R. Y. LIN, in Proc. Fourth Annual Conf. Fossil Energy Materials, edited by R. R. Judkins and D. N. Braski (U.S. Department of Energy, 1990) p. 475.
15. F. GESMUNDO, Y. NIU, F. VIANI and O. TASSA, *J. Phys.* **IV C9** (1993) 375.
16. M. A. E. MEDINA, M. CASALES, A. M. VILLAFANE, J. P. CALDERON, L. MARTINEZ and J. G. G. RODRIGUEZ, *Mat. Sci. Engg.* A **300** (2001) 183.
17. K. L. LUTHRA and D. A. SHORES, *J. Electrochem. Soc.* **127** (1980) 2202.
18. J. A. GOEBEL and F. S. PETTIT, *Met. Trans.* **1** (1970) 1943.
19. P. KOFSTAD, "High Temperature Corrosion" (Elsevier Applied Science, New York, 1988) p. 465.

Received 3 April
and accepted 13 November 2001